

DPmoire: A tool for constructing accurate machine learning force fields in moiré systems

Jiaxuan Liu,^{1, 2} Zhong Fang,^{1, 2, 3} Hongming Weng,^{1, 2, 3, *} and Quansheng Wu^{1, 2, †}

¹*Beijing National Laboratory for Condensed Matter Physics and Institute of Physics, Chinese Academy of Sciences, Beijing 100190, China*

²*University of Chinese Academy of Sciences, Beijing 100049, China*

³*Songshan Lake Materials Laboratory, Dongguan, Guangdong 523808, China*

(Dated: February 18, 2025)

In moiré systems, the impact of lattice relaxation on electronic band structures is significant, yet the computational demands of first-principles relaxation are prohibitively high due to the large number of atoms involved. To address this challenge, we introduce a robust methodology for the construction of machine learning potentials specifically tailored for moiré structures and present an open-source software package **DPmoire** designed to facilitate this process. Utilizing this package, we have developed machine learning force fields (MLFFs) for MX_2 ($M = Mo, W$; $X = S, Se, Te$) materials. Our approach not only streamlines the computational process but also ensures accurate replication of the detailed electronic and structural properties typically observed in density functional theory (DFT) relaxations. The MLFFs were rigorously validated against standard DFT results, confirming their efficacy in capturing the complex interplay of atomic interactions within these layered materials. This development not only enhances our ability to explore the physical properties of moiré systems with reduced computational overhead but also opens new avenues for the study of relaxation effects and their impact on material properties in two-dimensional layered structures.

I. INTRODUCTION

In recent years, two-dimensional twisted moiré structures have captured significant interest due to the diverse physical phenomena they exhibit. By varying the inter-layer twist angle, researchers can tune the band structure of these materials, enabling the experimental observation of novel phenomena. For instance, in twisted graphene, when the twist angle reaches the so-called "magic angle," the valence band flattens, prompting electrons to transition from a weakly correlated to a strongly correlated state. This shift gives rise to a host of intriguing behaviors, including unconventional superconductivity, Mott insulating states, and the quantum anomalous Hall effect[1–12]. Similar phenomena have also been observed in moiré bilayers of transition metal dichalcogenides (TMDs)[13–19].

In twisted structures, the moiré potential narrows the bandwidth as the periodicity of the structure increases. For instance, the bandwidth of bilayer twisted graphene at a twist angle of 1.08° is only a few meV[4, 20], while the bandwidth of bilayer twisted $MoTe_2$ at 3.89° is just over 10 meV[14]. Such narrow bands are highly susceptible to the effects of lattice relaxation, which significantly influences their electronic properties. Theoretical calculations reveal that the electronic band structures of rigid twisted graphene differ markedly from those of relaxed systems[20]. Additionally, experimental studies using scanning tunneling microscopy (STM) have also doc-

umented the relaxation patterns in TMDs resulting from lattice reconstruction[21, 22].

To accurately model the electronic properties of moiré structures, density functional theory (DFT) is often employed, particularly for structures with large twist angles, where it is considered essential for reliable structural relaxation [14, 15, 19]. However, despite its high level of accuracy, the computational complexity of DFT scales cubically with the number of atoms, rendering it impractical for smaller-angle structures due to the sheer number of atoms involved.

To address this computational challenge, researchers have developed parameterized continuum models that are better suited for structures with small twist angles [23–30]. While these models provide a computationally feasible alternative, they typically do not reach the accuracy levels of DFT relaxation. For materials such as graphene [31–33] and transition metal dichalcogenides (TMDs) [34], empirical force fields have been effectively utilized for structural relaxation [12, 35–38]. However, in other systems, robust and extensively validated empirical potentials remain scarce, limiting the scope of studies that can be conducted.

Machine learning force fields (MLFF) offer a promising solution to the computational challenges posed by moiré structures[39–50]. Recent advancements in universal MLFFs have shown great promise in terms of versatility, efficiency, and accuracy for materials discovery and high-throughput calculations [51–56]. However, in the context of moiré systems, the energy scales of electronic bands are often on the order of millielectron volts (meV), a range comparable to the accuracy limits of these universal MLFFs. This indicates that while universal MLFFs provide broad applicability, their precision may be insuf-

* hmweng@iphy.ac.cn

† quansheng.wu@iphy.ac.cn

ficient for structural relaxation tasks in moiré systems, necessitating the development of MLFFs specifically tailored to individual material systems.

Previous efforts have successfully constructed MLFFs for twisted structures, achieving encouraging outcomes. Some studies have developed MLFFs for large twist angles and then applied these models to smaller angles [57, 58], while others have trained MLFFs on non-twisted structures before using them to relax twisted configurations [14, 59]. Additionally, a few approaches have combined initial training on non-twisted structures with subsequent transfer learning on large twist-angle structures to efficiently relax twisted configurations [60, 61]. This multifaceted strategy highlights the adaptability of MLFFs in addressing the specific challenges posed by the diverse configurations encountered in moiré systems.

While these innovative approaches have shown promise, their validation has often been limited to specific materials, and a comprehensive tool for constructing MLFFs tailored to twisted structures is still lacking. Moiré systems offer a unique platform for exploring novel phenomena such as strong correlations and topological states, with numerous experimental and theoretical advances highlighting their potential. Given the rapid development in this field, there is a pressing need for a universal tool that can conveniently and efficiently construct MLFFs for such complex systems. To bridge this gap, we propose a new methodology and introduce an open-source software, *DPmoire*, designed specifically for moiré systems. *DPmoire* leverages non-twisted structures to construct training datasets, facilitating the automated generation of MLFFs tailored to the unique challenges of moiré systems. This tool aims to streamline the MLFF construction process, enabling researchers to more effectively study and model the intricate behaviors exhibited by twisted materials.

II. METHODS

A. Moiré structures

Moiré twisted materials could be constructed by either applying a twist angle between layers of two layered materials or stacking two materials with a slight lattice constant mismatch. Generally, the smaller the twist angle, the larger the resulting moiré supercell. Different regions of a moiré structure exhibit various stacking arrangements. Taking twisted AA WSe₂ as an example (Fig. 1), in the AA region, the W/Se atoms in the top layer are aligned with the corresponding W/Se atoms in the bottom layer. In the MX region, the W atoms in the top layer align with the Se atoms in the bottom layer, while in the XM region, the Se atoms in the top layer align with the W atoms in the bottom layer. In non-twisted structures, various stacking configurations correspond to different energy states, as illustrated in Fig. 1(b). When the interlayer twist angle is minimal, the

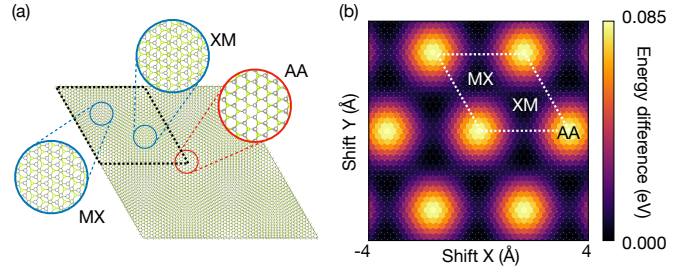


FIG. 1. (a) Moiré crystal structure of WSe₂ with a 2.13° AA stacking twist, resembling the atomic layout of non-twisted bilayer WSe₂. (b) Energy profile of non-twisted bilayer WSe₂ based on relative in-plane shifts between layers, where X and Y axes represent shift vectors, and color indicates unit cell energy. Energy at MX and XM stackings is zeroed. Interlayer distance is 6.8 Å.

lattice vectors of both layers closely match, making the local atomic configurations in the moiré structure similar to those in non-twisted structures. By modeling the potential energy surfaces of these non-twisted configurations, we can effectively reconstruct the potential energy landscape of twisted structures, thereby advancing our understanding of their unique properties.

B. Machine learning force fields

Machine learning force field (MLFF) [39–50] refers to machine learning algorithms for predicting the energy and forces of crystal structures. Typically, to train an MLFF, it needs a dataset consisting of a set of crystal structures along with their corresponding energies and forces. Once training is complete, the MLFF can rapidly predict the energies and forces of similar structures. The computational cost of MLFF prediction scales linearly with the number of atoms, making the cost of relaxation manageable even for very large structures.

However, constructing a comprehensive dataset can be a time-consuming endeavor. Directly using ab-initio molecular dynamics (MD) simulations to build datasets is a relatively inefficient approach, as structures that are close in time within an MD trajectory are very similar. This similarity results in a redundancy that offers little added value to the training dataset, posing a challenge for efficient MLFF deployment.

On-the-fly machine learning force field (MLFF) approaches like DP-GEN[62] and the MLFF module of the Vienna Ab initio Simulation Package (VASP)[39, 63] provide effective solutions for managing computational costs in molecular dynamics (MD) simulations. This article focuses on the MLFF module within VASP. This module automates the process of data collection, MLFF training, and its immediate application to accelerate MD simulations within a continuous loop. The MLFF module operates based on Bayesian linear regression, which allows it to directly estimate the error in its predictions

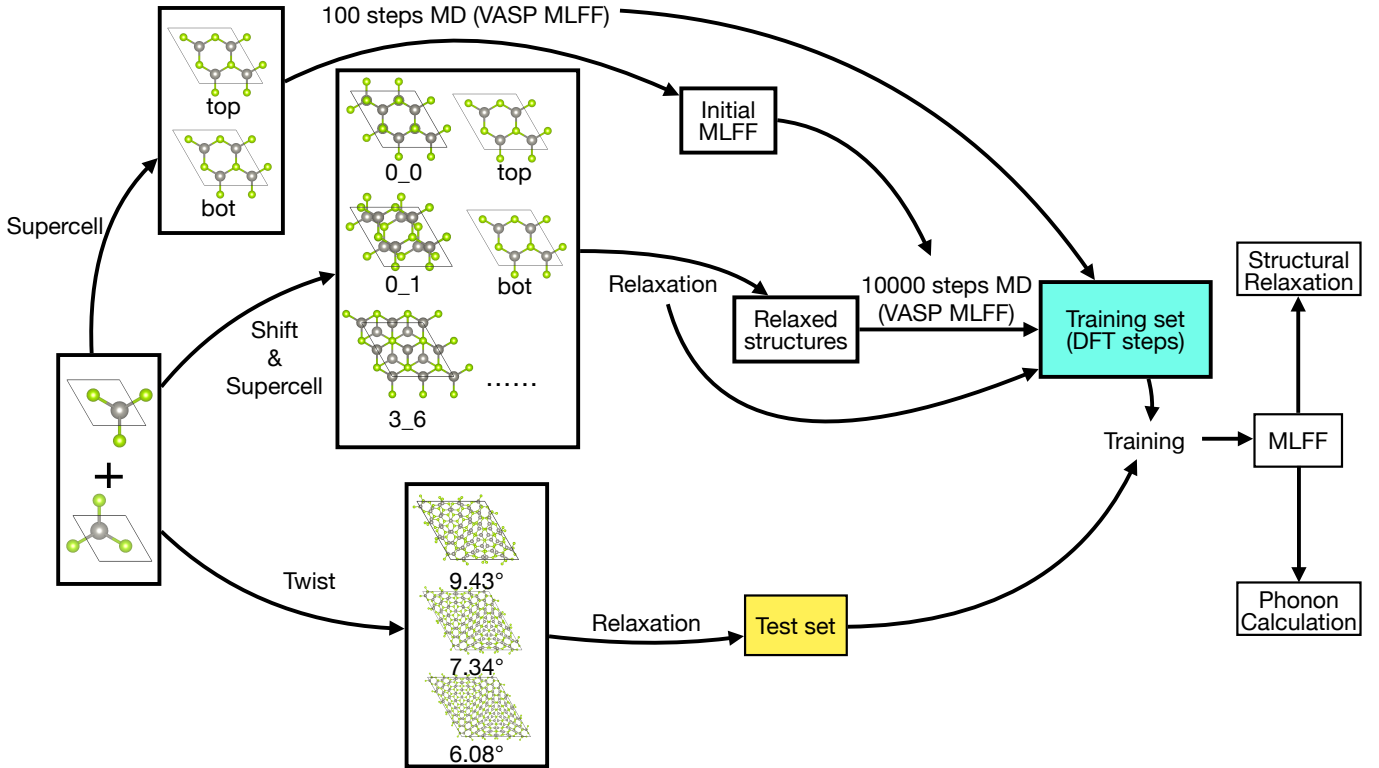


FIG. 2. Schematic overview of the process for constructing a Machine Learning Force Field (MLFF) for moiré systems. Initially, an MLFF is generated for monolayer structures to stabilize subsequent molecular dynamics (MD) simulations for bilayer systems. We then create non-twisted bilayer structures with various stacking configurations, relax these structures, and run MD simulations using the VASP MLFF module to construct the training dataset. The coordinates (x and y) of a selected atom from each layer are maintained constant during relaxation to preserve the integrity of the stacking order. Subsequently, the twisted structures are relaxed using density functional theory (DFT) to generate the test dataset. The MLFF is ultimately trained on these collected datasets, ensuring it can accurately predict the physical behaviors of moiré systems.

without needing to compare them against ab-initio results. During an MD simulation, if the module estimates a small error, it applies the MLFF-predicted results directly. Conversely, if a large error is estimated, it discards these results and performs a density functional theory (DFT) step to obtain accurate data. This ab-initio data is then added to the training dataset for refining the MLFF. This iterative process repeats throughout the MD simulation, allowing for extensive sampling from MD trajectories, which could involve hundreds of thousands of steps, while only requiring DFT calculations for a fraction of those steps. As a result, a high-quality dataset can be constructed with minimal computational expense, optimizing both resources and time.

The MLFF algorithm in VASP is designed to be relatively lightweight, which significantly reduces the training time required during the simulation loop. However, this streamlined approach means that the accuracy of the VASP MLFF may not rival that of more complex neural network-based MLFF algorithms. Consequently, we utilize the VASP MLFF primarily for dataset generation, subsequently employing a more accurate neural network-based MLFF to fit the data collected.

One such advanced approach is NequIP, a machine

learning force field based on an E(3)-equivariant graph neural network[41]. This method ensures covariance among the inputs, outputs, and hidden layers, leading to enhanced data efficiency and model accuracy. Another notable E(3)-equivariant algorithm is Allegro, which is particularly well-suited for large structures and optimized for parallel computing[40]. While this article primarily focuses on the application of Allegro, the dataset generated using our approach is versatile and can be employed to train other MLFF models as well. This flexibility facilitates the exploration and application of various advanced MLFF techniques in computational material science.

C. MLFF for moiré systems

To develop a machine-learned force field (MLFF) for moiré superlattice structures, we initially constructed 2×2 supercells of non-twisted bilayers and introduced in-plane shifts to generate various stacking configurations. Subsequently, structural relaxations were performed for each configuration, ensuring that the x and y coordinates of a reference atom from each layer remained fixed

to prevent structural drift toward energetically favorable stackings. The lattice constants were also held constant throughout the simulations. The relaxation data were compiled into a training dataset.

Following the relaxation phase, Molecular Dynamics (MD) simulations were conducted under the aforementioned constraints to augment the training data pool. For these simulations, we employed the VASP MLFF module to explore a wide range of atomic configurations, selectively incorporating data solely from density functional theory (DFT) calculation steps. Given the potential instability when initiating MD simulations with VASP MLFF from an untrained state, we initially established a baseline MLFF using single-layer structures before proceeding with the full simulations. To ensure the MLFF's applicability to moiré systems and to mitigate overfitting to non-twisted structures, we constructed the test set using large-angle moiré patterns. These were subjected to ab initio relaxations, with the resultant data serving as the test set.

Finally, the compilation of the aforementioned datasets facilitated the training of a robust and accurate MLFF. While we utilized the Allegro framework for MLFF training in this study, other MLFF algorithms, such as DeepMD[42], could also be effectively trained on these datasets to potentially enhance predictive accuracy and transferability across similar complex structures.

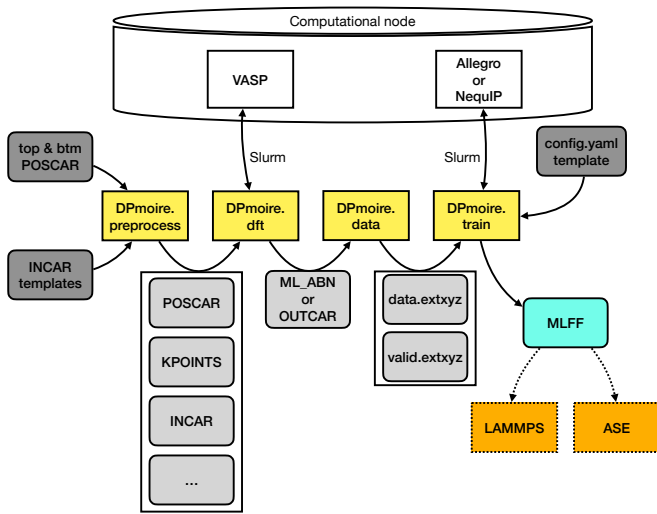


FIG. 3. Overview of the DPmoire package workflow. Initially, the **preprocess** module utilizes the provided POSCAR files for each layer along with an INCAR template to generate the necessary input files for subsequent VASP DFT calculations. The **dft** module then orchestrates these calculations using the Slurm management system. Upon completion, the **data** module collects the results and compiles them into datasets formatted in **extxyz**. Subsequently, the **train** module begins training a machine learning force field using these datasets, adhering to the parameters specified in the MLFF configuration template file. Once trained, the MLFF can be integrated with software packages such as LAMMPS[64] or ASE[65] to facilitate structural relaxation.

Eventually, the procedure described above was implemented in DPmoire. As shown in Fig.3, DPmoire is structured into four functional modules: DPmoire.preprocess, DPmoire.dft, DPmoire.data and DPmoire.train. Firstly, as provided the unit cell structures of each layer, DPmoire.preprocess module will automatically combine two layers and generate shifted structures of a 2×2 supercell. The twisted structure for building test set will also be prepared. The preprocess module will take care of the input files for VASP according to the provided templates. After that, the DPmoire.dft module will submit VASP calculation jobs through slurm system. When all the calculation is done, the DFT-calculated data in ML_ABN and OUTCAR files will be collected by DPmoire.data module. Then, DPmoire.data will generate the training set file (data.extxyz) and test set file (valid.extxyz). This format can be directly read by Allegro and NequiP packages. DPmoire.train module will modify the system-dependent settings in configuration file according to given template for training Allegro or NequiP MLFF, and submit the training job. After the training is done, the trained MLFF can be used in ASE[65] or LAMMPS[64] to perform structural relaxation.

III. RESULTS

The accuracy of machine-learned force fields (MLFF) is critically dependent on the precision of underlying density functional theory (DFT) calculations. Particularly in layered materials, the van der Waals (vdW) interactions play a crucial role in determining the DFT-calculated interlayer distances, making their inclusion indispensable. Over the years, a plethora of vdW correction methodologies have been developed [66–82]. Despite these developments, the predicted interlayer distances using different vdW corrections can vary by a few tenths of an Ångstrom.

Given this variation, it is crucial to identify the most appropriate vdW correction for each material prior to the training of MLFFs. To this end, we evaluated the lattice constants obtained under various vdW corrections, comparing them against experimental measurements to ascertain the optimal vdW correction for each material. The details of this comparative analysis are documented in Appendix A, providing a rigorous foundation for the subsequent MLFF training. Typically, for TMDs, our findings indicate that the DFT-D3 method with a zero-damping function (IVDW=11), as developed by Grimme[76], provides the optimal vdW correction for MoS₂ and WSe₂. The vdW-DF-cx method[69] proves most effective for MoSe₂ and WS₂. For MoTe₂, the DFT-D2 method (IVDW=10) from Grimme[75] yields the best results, while the SCAN+rVV10 correction[71] is found to be the optimal vdW correction for WTe₂. These tailored corrections are crucial for enhancing the accuracy of DFT calculations, thereby improving the robustness

of the developed MLFFs for different TMD materials.

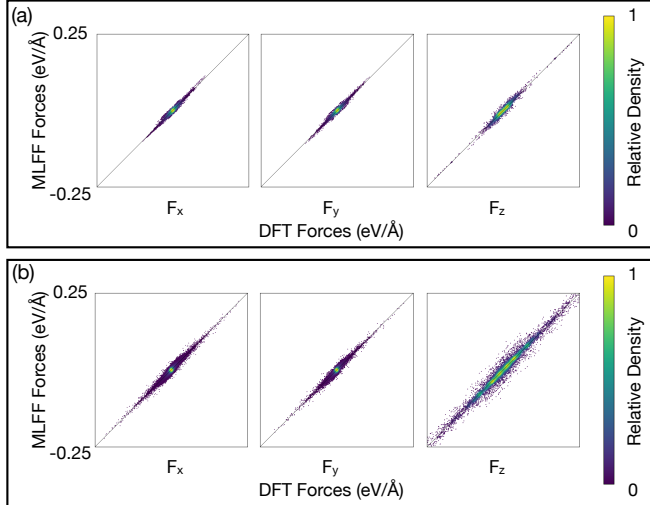


FIG. 4. (a) MLFF-predicted versus DFT-calculated forces for AA WSe₂ at a 7.34° twist. (b) Similar comparison for AA MoS₂ across 9.34°, 7.34°, and 6.08° twists. These panels illustrate the MLFFs fidelity in capturing force dynamics under different twisting conditions.

Then, the MLFF is constructed utilizing the previously determined optimal vdW corrections for both AA and AB stacking configurations of MX₂ (M = Mo, W; X = S, Se, Te) materials, as thoroughly discussed in Appendix B. We specifically examined AA WSe₂ and AA MoS₂ as representative examples. The efficacy of the MLFF is demonstrated through a comparison of predicted and DFT-calculated forces within the test set, as illustrated in Fig. 4. The comparison shows a strong alignment between the MLFF predictions and the DFT calculations, with root mean square errors of 0.007 eV/Å and 0.014 eV/Å for WSe₂ and MoS₂, respectively, underscoring the accuracy of the MLFF in capturing the essential physical interactions in these materials.

We further evaluated the performance of the trained MLFFs by relaxing a structure with a 7.34° twist angle, followed by a comparison relaxation using DFT. As depicted in Fig. 5, the relaxation outcomes from the MLFF are nearly indistinguishable from those obtained via DFT, with no significant deviations observed. The maximum differences in atomic positions were found to be 0.039 Å in WSe₂ and 0.003 Å in MoS₂. In the relaxed structures, regions characterized by MX and XM stacking exhibited lower interlayer distances compared to the AA regions. Throughout the relaxation process, atoms near the AA regions tend to rotate counterclockwise, which intensifies the local twist effect. Conversely, atoms in proximity to the MX and XM regions rotate clockwise. This differential rotation behavior strategically maximizes the area of MX and XM regions while minimizing the AA region. These findings align well with previous theoretical studies [23].

We also performed band structure calculations on both

MLFF-relaxed and DFT-relaxed structures for AA WSe₂ and AA MoS₂, as shown in Fig. 6. The band structures of the two methods are nearly identical, with only minor differences, demonstrating that the MLFF is sufficiently accurate to capture the essential physical phenomena in moiré structures without the need for additional DFT relaxation. As detailed in Appendix B, MLFFs for other materials also exhibited robust performance. For MoS₂ (Figs. A1, A2), WS₂ (Figs. A7, A8), AB MoTe₂ (Fig. A6), and WTe₂ (Figs. A11, A12), the structures relaxed by MLFF and DFT methods were nearly identical, and their corresponding band structures closely matched. However, for materials like MoSe₂ (Figs. A3, A4) and AA-stacked MoTe₂ (Fig. A5), slight variations in interlayer distances led to minor differences in their band structures. We further analyzed the 5.09° twist angle in AA and AB stacked MoSe₂ (Fig. A13), where the discrepancies between DFT-relaxed and MLFF-relaxed structures were reduced, suggesting that the observed suboptimal performance in these materials may be due to the larger twist angles.

IV. CONCLUSION

In this work, we introduced a universal methodology and developed an open-source tool, DPmoire, for constructing machine-learned force fields (MLFF) tailored to moiré structures. Utilizing the VASP MLFF module, DPmoire effectively generates training sets and constructs validation sets based on large-twist-angle configurations. We successfully trained accurate MLFFs for MX₂ (M = Mo, W; X = S, Se, Te) systems, which precisely replicate both the relaxation patterns and electronic band structures observed in DFT relaxations, but at a significantly reduced computational cost.

This innovative tool enables the effective relaxation of moiré systems across a broader range of smaller angles and varied materials. Additionally, it facilitates phonon calculations within these complex systems. We anticipate that DPmoire will significantly enhance the understanding of physical phenomena influenced by relaxation effects and spur the discovery of novel moiré materials.

V. CODE AVAILABILITY

The code for DPmoire is publicly available on GitHub at this link <https://github.com/JiaxuanLiu-Arsko/DPmoire>. MLFFs for TMDs can be accessed at this release <https://github.com/JiaxuanLiu-Arsko/DPmoire/releases/tag/v1.0.0>.

ACKNOWLEDGMENTS

J.L. thank Hanqi Pi for helpful discussions. This work was supported by the Science Center of the National Nat-

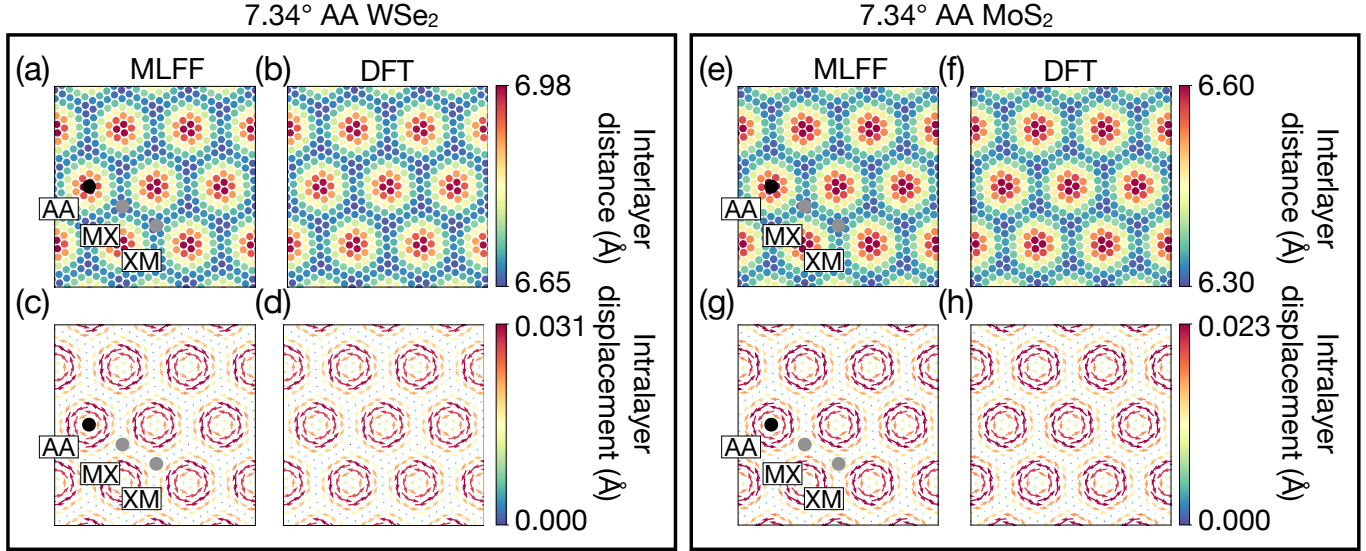


FIG. 5. Relaxation pattern of 7.34° AA twisted bilayer WSe₂. (a) and (b) correspond to the interlayer distance and intralayer displacement in MLFF-relaxed structure, respectively. (c) and (d) correspond to the interlayer distance and intralayer displacement in DFT-relaxed structure, respectively.

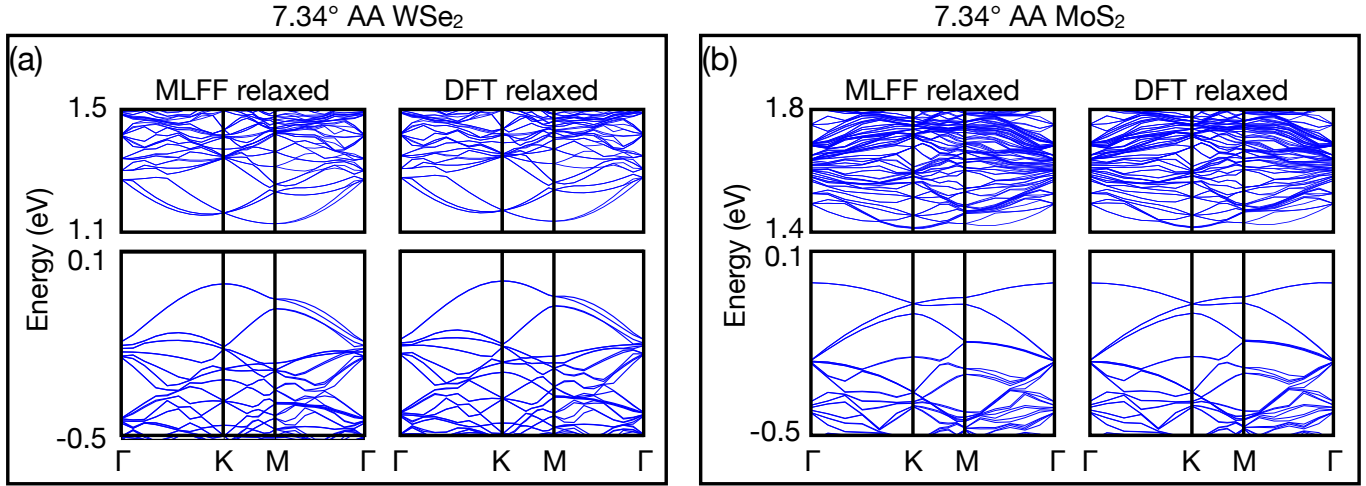


FIG. 6. (a), Comparison of electronic band structure between MLFF-relaxed structure and DFT-relaxed structure in 7.34° AA WSe₂. (b), Comparison of electronic band structure between MLFF-relaxed structure and DFT-relaxed structure in 7.34° AA MoS₂.

ural Science Foundation of China (Grant No. 12188101), the National Key R&D Program of China (Grant No. 2023YFA1607400, 2024YFA1408400, 2022YFA1403800), the National Natural Science Foundation of China (Grant No.12274436, 11925408, 11921004), and H.W. acknowledge support from the New Cornerstone Science Foundation through the XPLORER PRIZE.

Appendix A: van der Waals corrections

For layered materials, the choice of van der Waals correction significantly affects the relaxation results. Therefore, before training the MLFF, we performed DFT relax-

ation on the bulk structure of each material using different van der Waals corrections. We compared the relaxed lattice constants with the experimental lattice constants from the ICSD [83] to select the optimal lattice constant.

Appendix B: MLFF of transition metal dichalcogenides

We used DPmoire to construct MLFFs for bilayer twisted MX₂ (M = Mo, W; X = S, Se, Te), and the results are presented in this section.

We constructed MLFFs for AA and AB stacking of different materials. To verify the reliability of the MLFFs,

	experiment	optB86[67]	optB88[68]	vdW-DF[66]	vdW-DF-cx[69]
a,b(Å)	3.160	3.166	3.192	3.235	3.150
c(Å)	12.294	12.376	12.466	13.108	12.270
	optPBE-vdW[68]	rVV10[70]	SCAN+rVV10[71]	r ² SCAN+rVV10[72]	-
a,b(Å)	3.201	3.178	3.169	3.175	-
c(Å)	12.717	12.130	12.456	12.427	-
	rev-vdW-DF2[73]	vdW-DF2[74]	IVDW=10	IVDW=11	IVDW=12
a,b(Å)	3.167	3.284	3.188	3.161	3.148
c(Å)	12.342	12.872	12.413	12.336	12.084
	IVDW=20	IVDW=21	IVDW=263	IVDW=4	IVDW=3
a,b(Å)	3.157	3.167	3.141	3.160	3.173
c(Å)	12.052	12.097	12.234	12.541	12.900

TABLE A1. Relaxaed lattice constant of bulk MoS₂ using different van der Waals corrections. Experimental data comes from ICSD 49801. Here IVDW=10 is the DFT-D2 method of Grimme[75]. IVDW=11 is the DFT-D3 method of Grimme with zero-damping function[76]. IVDW=12 is the DFT-D3 method with Becke-Johnson damping function [77]. IVDW=20 is the Tkatchenko-Scheffler method[78]. IVDW=263 is the Many-body dispersion energy with fractionally ionic model for polarizability method [79, 80]. IVDW=3 is the DFT-ulg method[81]. IVDW=4 is the dDsC dispersion correction[82]

	experiment	optB86	optB88	vdW-DF	vdW-DF-cx
a,b(Å)	3.288	3.299	3.330	3.382	3.279
c(Å)	12.92	13.044	13.161	13.881	12.911
	optPBE-vdW	rVV10	SCAN+rVV10	r ² SCAN+rVV10	-
a,b(Å)	3.341	3.316	3.295	3.308	-
c(Å)	13.432	12.864	13.164	13.107	-
	rev-vdW-DF2	vdW-DF2	IVDW=10	IVDW=11	IVDW=12
a,b(Å)	3.300	3.444	3.315	3.291	3.276
c(Å)	13.020	13.672	13.021	13.011	12.721
	IVDW=20	IVDW=21	IVDW=263	IVDW=4	IVDW=3
a,b(Å)	3.290	3.296	3.271	3.293	3.307
c(Å)	12.760	12.740	12.834	13.181	13.497

TABLE A2. Relaxaed lattice constant of bulk MoSe₂ using different van der Waals corrections. Experimental data comes from ICSD 644335.

we compared the forces calculated by the MLFFs with those from DFT on a test set. Additionally, we constructed a 7.34° twisted structure and performed relaxation using both the MLFF and DFT, comparing the interlayer distance and intralayer displacement after relaxation by the different methods. Finally, we calculated the band structures of the structures relaxed by both methods.

	experiment	optB86	optB88	vdW-DF	vdW-DF-cx
a,b(Å)	3.521	3.527	3.567	3.631	3.502
c(Å)	13.96	14.032	14.213	15.007	13.867
	optPBE-vdW	rVV10	SCAN+rVV10	r ² SCAN+rVV10	PBE
a,b(Å)	3.580	3.546	3.503	3.542	3.551
c(Å)	14.475	13.949	14.223	14.187	15.095
	rev-vdW-DF2	vdW-DF2	IVDW=10	IVDW=11	IVDW=12
a,b(Å)	3.529	3.711	3.519	3.512	3.490
c(Å)	14.028	14.891	13.976	13.984	13.649
	IVDW=20	IVDW=21	IVDW=263	IVDW=4	IVDW=3
a,b(Å)	3.514	3.516	3.490	3.515	3.531
c(Å)	13.923	13.826	13.709	14.047	14.222

TABLE A3. Relaxaed lattice constant of bulk MoTe₂ using different van der Waals corrections. Experimental data comes from ICSD 644476.

	experiment	optB86	optB88	vdW-DF	vdW-DF-cx
a,b(Å)	3.14	3.167	3.191	3.232	3.152
c(Å)	12.3	12.431	12.516	13.158	12.332
	optPBE-vdW	rVV10	SCAN+rVV10	r ² SCAN+rVV10	-
a,b(Å)	3.200	3.179	3.155	3.167	-
c(Å)	12.777	12.186	12.509	12.482	-
	rev-vdW-DF2	vdW-DF2	IVDW=10	IVDW=11	IVDW=12
a,b(Å)	3.167	3.278	3.180	3.166	3.149
c(Å)	12.393	12.913	12.139	12.415	12.125
	IVDW=20	IVDW=21	IVDW=263	IVDW=4	IVDW=3
a,b(Å)	3.160	3.168	3.149	3.159	3.172
c(Å)	12.232	12.223	12.464	12.584	12.979

TABLE A4. Relaxaed lattice constant of bulk WS₂ using different van der Waals corrections. Experimental data comes from ICSD 49801.

	experiment	optB86	optB88	vdW-DF	vdW-DF-cx
a,b(Å)	3.285	3.298	3.327	3.377	3.279
c(Å)	12.961	13.107	13.220	13.907	12.981
	optPBE-vdW	rVV10	SCAN+rVV10	r ² SCAN+rVV10	-
a,b(Å)	3.338	3.314	3.282	3.298	-
c(Å)	13.486	12.931	13.205	13.163	-
	rev-vdW-DF2	vdW-DF2	IVDW=10	IVDW=11	IVDW=12
a,b(Å)	3.298	3.436	3.307	3.285	3.275
c(Å)	13.081	13.711	12.779	12.998	12.775
	IVDW=20	IVDW=21	IVDW=263	IVDW=4	IVDW=3
a,b(Å)	3.291	3.296	3.276	3.289	3.305
c(Å)	12.956	12.886	13.058	13.224	13.568

TABLE A5. Relaxaed lattice constant of bulk WSe₂ using different van der Waals corrections. Experimental data comes from ICSD 652167.

	experiment	optB86	optB88	vdW-DF	vdW-DF-cx
a,b(Å)	3.491	3.530	3.570	3.632	3.505
c(Å)	14.31	14.115	14.278	15.042	13.950
	optPBE-vdW	rVV10	SCAN+rVV10	r ² SCAN+rVV10	-
a,b(Å)	3.582	3.547	3.498	3.539	-
c(Å)	14.538	14.019	14.268	14.234	-
	rev-vdW-DF2	vdW-DF2	IVDW=10	IVDW=11	IVDW=12
a,b(Å)	3.531	3.711	3.552	3.510	3.494
c(Å)	14.105	14.904	13.788	14.003	13.716
	IVDW=20	IVDW=21	IVDW=263	IVDW=4	IVDW=3
a,b(Å)	3.519	3.522	3.497	3.516	3.534
c(Å)	14.149	14.013	13.911	14.129	14.324

TABLE A6. Relaxaed lattice constant of bulk WTe₂ using different van der Waals corrections. Experimental data comes from ICSD 653170.

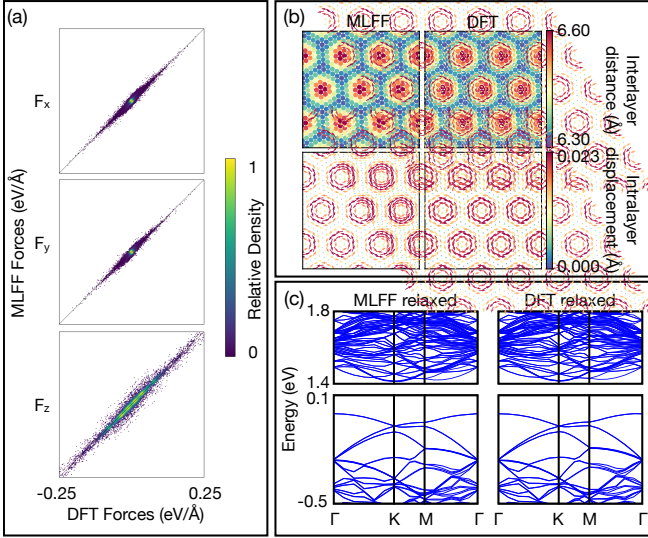


FIG. A1. Evaluation of 7.34° AA MoS₂. (a), Comparison between MLFF-predicted forces and DFT-calculated forces in test set. The x-axis shows the DFT-calculated force, and the y-axis shows the MLFF-calculated force. (b), Relaxation pattern of MLFF-relaxed structure and DFT-relaxed structure. Figs in first row are MLFF-relaxed structure; Figs in second row are DFT-relaxed structure. (c), Band structure of MLFF-relaxed structure and DFT-relaxed structure.

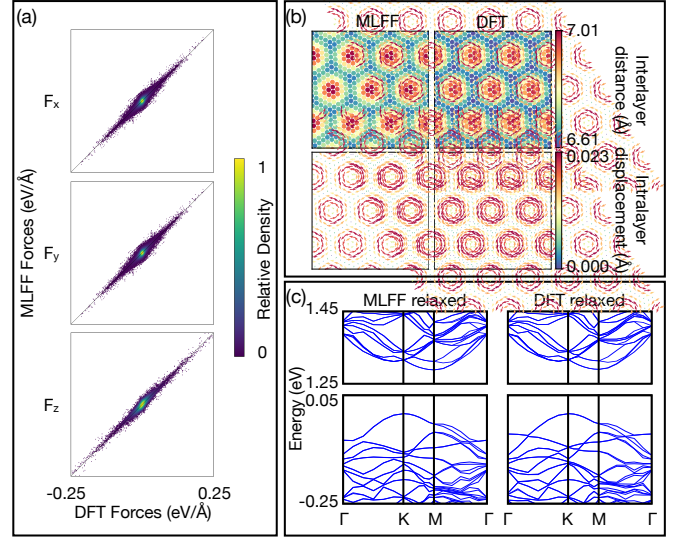


FIG. A3. Evaluation of 7.34° AA MoSe₂. (a), Comparison between MLFF-predicted forces and DFT-calculated forces in test set. The x-axis shows the DFT-calculated force, and the y-axis shows the MLFF-calculated force. (b), Relaxation pattern of MLFF-relaxed structure and DFT-relaxed structure. Figs in first row are MLFF-relaxed structure; Figs in second row are DFT-relaxed structure. (c), Band structure of MLFF-relaxed structure and DFT-relaxed structure.

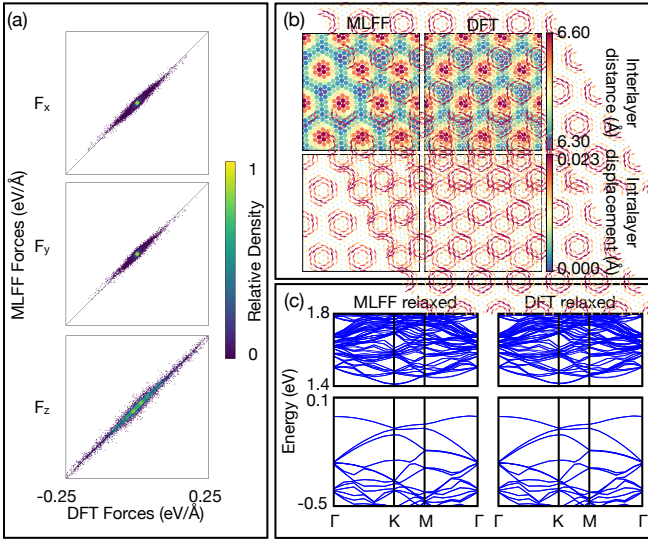


FIG. A2. Evaluation of 7.34° AB MoS₂. (a), Comparison between MLFF-predicted forces and DFT-calculated forces in test set. The x-axis shows the DFT-calculated force, and the y-axis shows the MLFF-calculated force. (b), Relaxation pattern of MLFF-relaxed structure and DFT-relaxed structure. Figs in first row are MLFF-relaxed structure; Figs in second row are DFT-relaxed structure. (c), Band structure of MLFF-relaxed structure and DFT-relaxed structure.

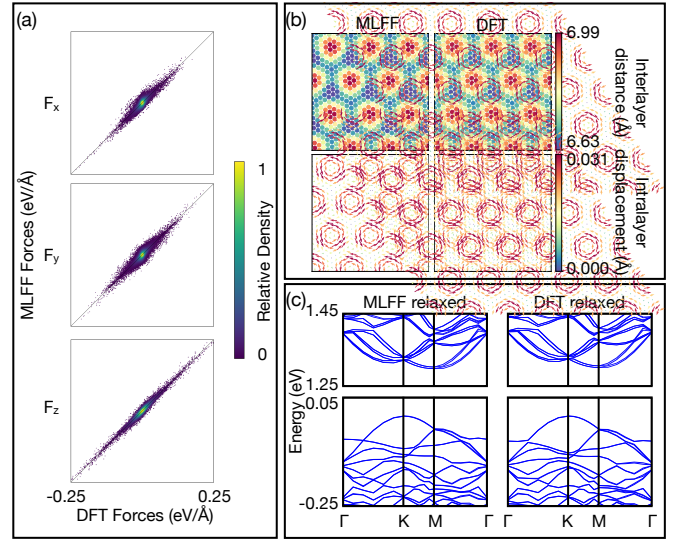


FIG. A4. Evaluation of 7.34° AB MoSe₂. (a), Comparison between MLFF-predicted forces and DFT-calculated forces in test set. The x-axis shows the DFT-calculated force, and the y-axis shows the MLFF-calculated force. (b), Relaxation pattern of MLFF-relaxed structure and DFT-relaxed structure. Figs in first row are MLFF-relaxed structure; Figs in second row are DFT-relaxed structure. (c), Band structure of MLFF-relaxed structure and DFT-relaxed structure.

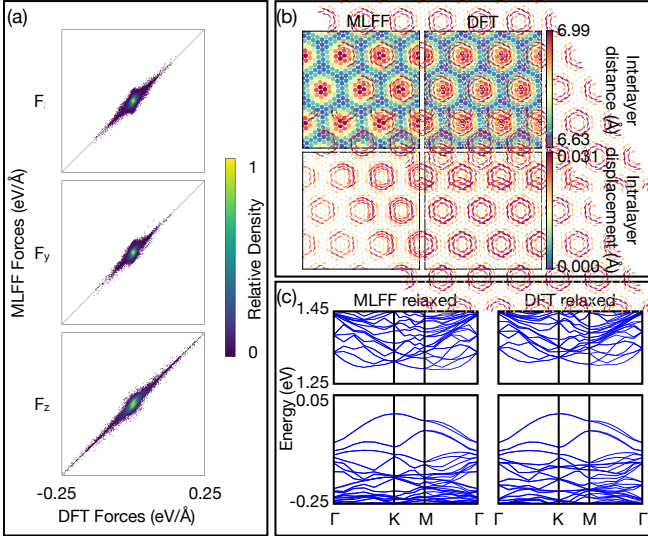


FIG. A5. Evaluation of 7.34° AA MoTe₂. (a), Comparison between MLFF-predicted forces and DFT-calculated forces in test set. The x-axis shows the DFT-calculated force, and the y-axis shows the MLFF-calculated force. (b), Relaxation pattern of MLFF-relaxed structure and DFT-relaxed structure. Figs in first row are MLFF-relaxed structure; Figs in second row are DFT-relaxed structure. (c), Band structure of MLFF-relaxed structure and DFT-relaxed structure.

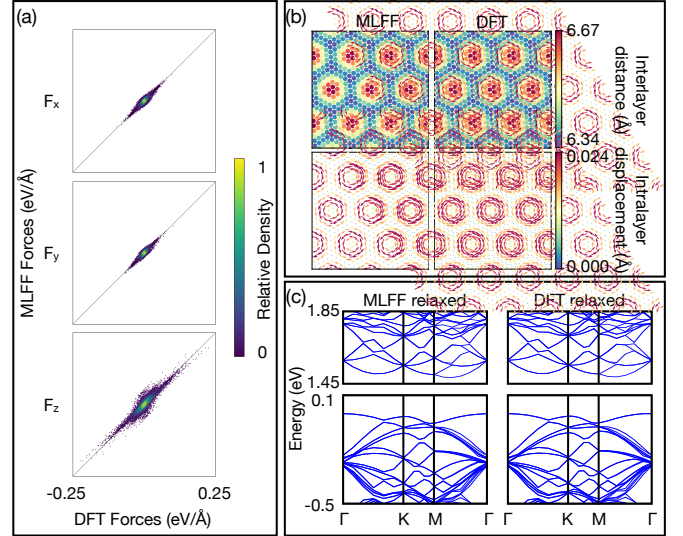


FIG. A7. Evaluation of 7.34° AA WS₂. (a), Comparison between MLFF-predicted forces and DFT-calculated forces in test set. The x-axis shows the DFT-calculated force, and the y-axis shows the MLFF-calculated force. (b), Relaxation pattern of MLFF-relaxed structure and DFT-relaxed structure. Figs in first row are MLFF-relaxed structure; Figs in second row are DFT-relaxed structure. (c), Band structure of MLFF-relaxed structure and DFT-relaxed structure.

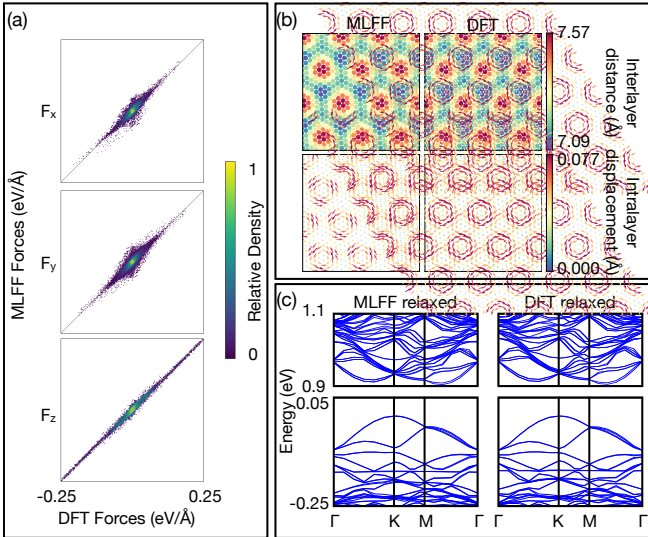


FIG. A6. Evaluation of 7.34° AB MoTe₂. (a), Comparison between MLFF-predicted forces and DFT-calculated forces in test set. The x-axis shows the DFT-calculated force, and the y-axis shows the MLFF-calculated force. (b), Relaxation pattern of MLFF-relaxed structure and DFT-relaxed structure. Figs in first row are MLFF-relaxed structure; Figs in second row are DFT-relaxed structure. (c), Band structure of MLFF-relaxed structure and DFT-relaxed structure.

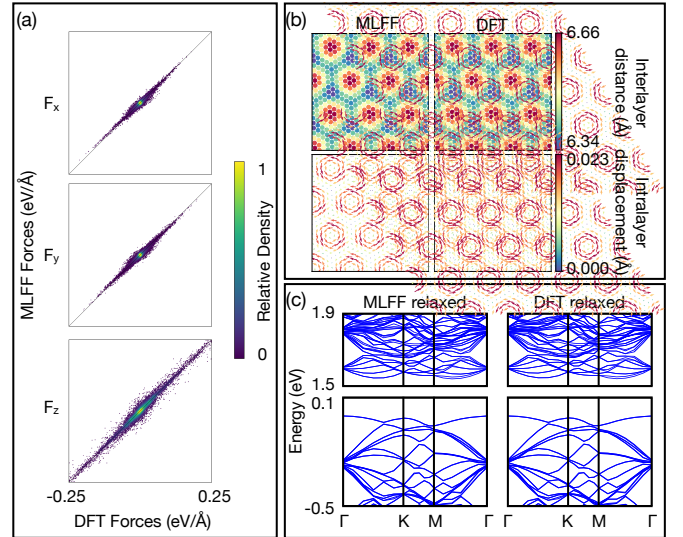


FIG. A8. Evaluation of 7.34° AB WS₂. (a), Comparison between MLFF-predicted forces and DFT-calculated forces in test set. The x-axis shows the DFT-calculated force, and the y-axis shows the MLFF-calculated force. (b), Relaxation pattern of MLFF-relaxed structure and DFT-relaxed structure. Figs in first row are MLFF-relaxed structure; Figs in second row are DFT-relaxed structure. (c), Band structure of MLFF-relaxed structure and DFT-relaxed structure.

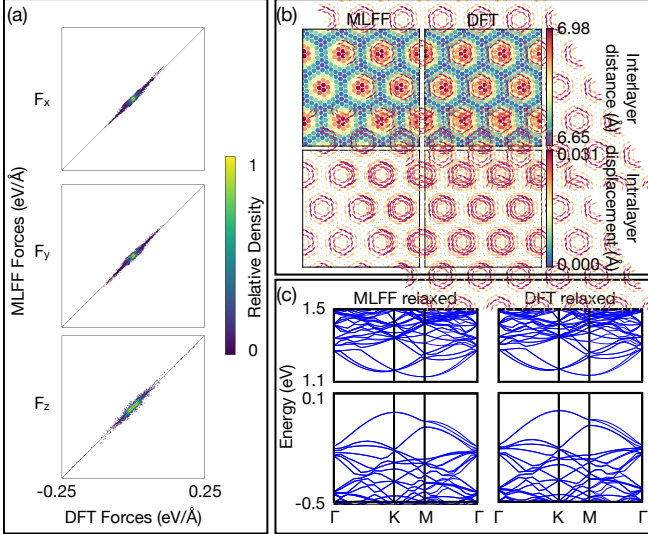


FIG. A9. Evaluation of 7.34° AA WSe₂. (a), Comparison between MLFF-predicted forces and DFT-calculated forces in test set. The x-axis shows the DFT-calculated force, and the y-axis shows the MLFF-calculated force. (b), Relaxation pattern of MLFF-relaxed structure and DFT-relaxed structure. Figs in first row are MLFF-relaxed structure; Figs in second row are DFT-relaxed structure. (c), Band structure of MLFF-relaxed structure and DFT-relaxed structure.

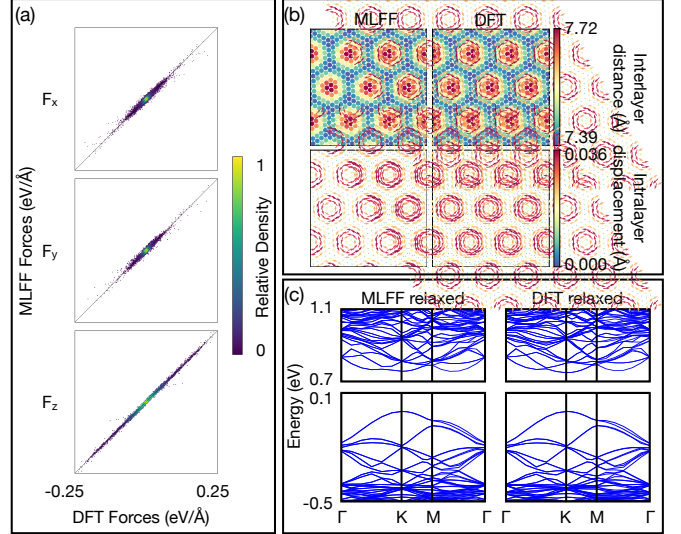


FIG. A11. Evaluation of 7.34° AA WTe₂. (a), Comparison between MLFF-predicted forces and DFT-calculated forces in test set. The x-axis shows the DFT-calculated force, and the y-axis shows the MLFF-calculated force. (b), Relaxation pattern of MLFF-relaxed structure and DFT-relaxed structure. Figs in first row are MLFF-relaxed structure; Figs in second row are DFT-relaxed structure. (c), Band structure of MLFF-relaxed structure and DFT-relaxed structure.

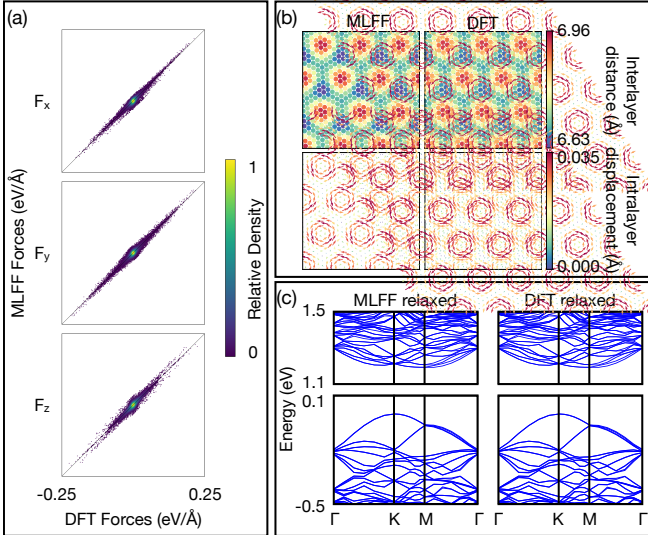


FIG. A10. Evaluation of 7.34° AB WSe₂. (a), Comparison between MLFF-predicted forces and DFT-calculated forces in test set. The x-axis shows the DFT-calculated force, and the y-axis shows the MLFF-calculated force. (b), Relaxation pattern of MLFF-relaxed structure and DFT-relaxed structure. Figs in first row are MLFF-relaxed structure; Figs in second row are DFT-relaxed structure. (c), Band structure of MLFF-relaxed structure and DFT-relaxed structure.

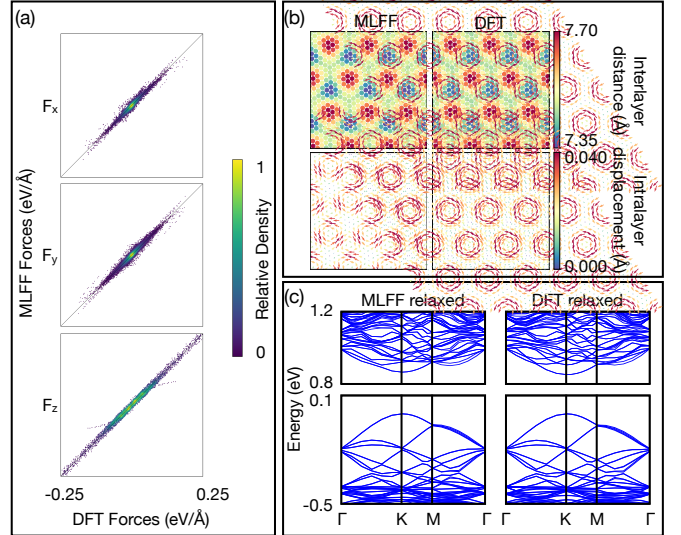


FIG. A12. Evaluation of 7.34° AB WTe₂. (a), Comparison between MLFF-predicted forces and DFT-calculated forces in test set. The x-axis shows the DFT-calculated force, and the y-axis shows the MLFF-calculated force. (b), Relaxation pattern of MLFF-relaxed structure and DFT-relaxed structure. Figs in first row are MLFF-relaxed structure; Figs in second row are DFT-relaxed structure. (c), Band structure of MLFF-relaxed structure and DFT-relaxed structure.

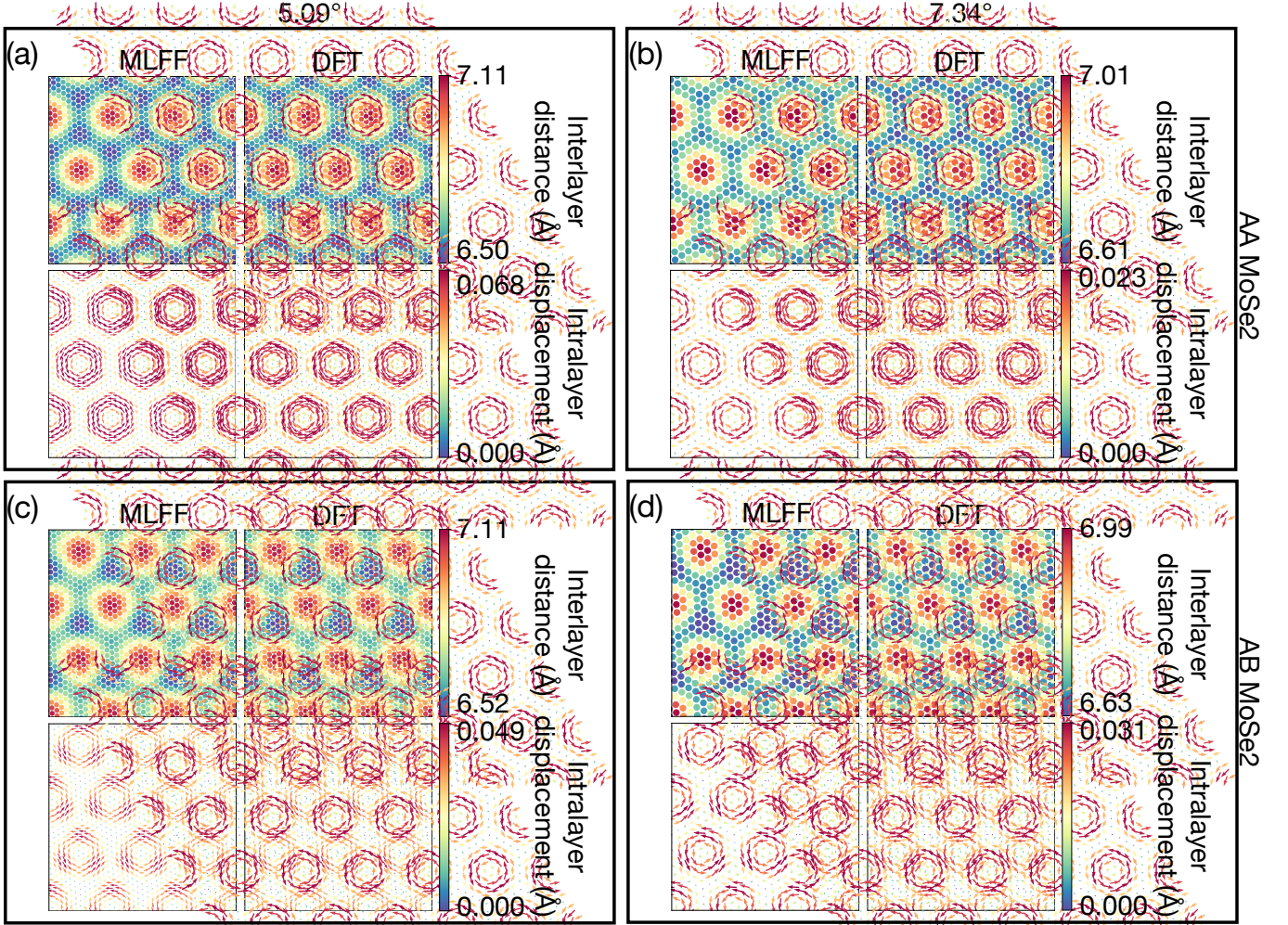


FIG. A13. Comparison between 5.09° and 7.34° MoSe₂. (a), Relaxation pattern of 5.09° MLFF-relaxed structure and DFT-relaxed AA MoSe₂. (b), Relaxation pattern of 7.34° MLFF-relaxed structure and DFT-relaxed AA MoSe₂. (c), Relaxation pattern of 5.09° MLFF-relaxed structure and DFT-relaxed AB MoSe₂. (d), Relaxation pattern of 7.34° MLFF-relaxed structure and DFT-relaxed AB MoSe₂.

[1] Y. Cao, V. Fatemi, S. Fang, K. Watanabe, T. Taniguchi, E. Kaxiras, and P. Jarillo-Herrero, Unconventional superconductivity in magic-angle graphene superlattices, *Nature* **556**, 43 (2018).

[2] Y. Cao, V. Fatemi, A. Demir, S. Fang, S. L. Tomarken, J. Y. Luo, J. D. Sanchez-Yamagishi, K. Watanabe, T. Taniguchi, E. Kaxiras, R. C. Ashoori, and P. Jarillo-Herrero, Correlated insulator behaviour at half-filling in magic-angle graphene superlattices, *Nature* **556**, 80 (2018).

[3] Y. Xie, A. T. Pierce, J. M. Park, D. E. Parker, E. Khalaf, P. Ledwith, Y. Cao, S. H. Lee, S. Chen, P. R. Forrester, K. Watanabe, T. Taniguchi, A. Vishwanath, P. Jarillo-Herrero, and A. Yacoby, Fractional Chern insulators in magic-angle twisted bilayer graphene, *Nature* **600**, 439 (2021).

[4] R. Bistritzer and A. H. MacDonald, Moir bands in twisted double-layer graphene, *Proceedings of the National Academy of Sciences* **108**, 12233 (2011).

[5] J. Liu, Z. Ma, J. Gao, and X. Dai, Quantum Valley Hall Effect, Orbital Magnetism, and Anomalous Hall Effect in Twisted Multilayer Graphene Systems, *Physical Review X* **9**, 031021 (2019).

[6] J. Liu and X. Dai, Theories for the correlated insulating states and quantum anomalous Hall effect phenomena in twisted bilayer graphene, *Physical Review B* **103**, 035427 (2021).

[7] X. Lu, P. Stepanov, W. Yang, M. Xie, M. A. Aamir, I. Das, C. Urgell, K. Watanabe, T. Taniguchi, G. Zhang, A. Bachtold, A. H. MacDonald, and D. K. Efetov, Superconductors, orbital magnets and correlated states in magic-angle bilayer graphene, *Nature* **574**, 653 (2019).

[8] A. Kerelsky, L. J. McGilly, D. M. Kennes, L. Xian, M. Yankowitz, S. Chen, K. Watanabe, T. Taniguchi, J. Hone, C. Dean, A. Rubio, and A. N. Pasupathy, Maximized electron interactions at the magic angle in twisted bilayer graphene, *Nature* **572**, 95 (2019).

[9] Y. Jiang, X. Lai, K. Watanabe, T. Taniguchi, K. Haule, J. Mao, and E. Y. Andrei, Charge order and broken rotational symmetry in magic-angle twisted bilayer graphene, *Nature* **573**, 91 (2019).

[10] M. Serlin, C. L. Tschirhart, H. Polshyn, Y. Zhang, J. Zhu, K. Watanabe, T. Taniguchi, L. Balents, and A. F. Young, Intrinsic quantized anomalous Hall effect in a moir heterostructure, *Science* **367**, 900 (2020).

[11] Y. Xie, B. Lian, B. Jck, X. Liu, C.-L. Chiu, K. Watanabe, T. Taniguchi, B. A. Bernevig, and A. Yazdani, Spectroscopic signatures of many-body correlations in magic-angle twisted bilayer graphene, *Nature* **572**, 101 (2019).

[12] C. Shen, Y. Chu, Q. Wu, N. Li, S. Wang, Y. Zhao, J. Tang, J. Liu, J. Tian, K. Watanabe, T. Taniguchi, R. Yang, Z. Y. Meng, D. Shi, O. V. Yazyev, and G. Zhang, Correlated states in twisted double bilayer graphene, *Nature Physics* **16**, 520 (2020).

[13] J. Cai, E. Anderson, C. Wang, X. Zhang, X. Liu, W. Holtzmann, Y. Zhang, F. Fan, T. Taniguchi, K. Watanabe, Y. Ran, T. Cao, L. Fu, D. Xiao, W. Yao, and X. Xu, Signatures of fractional quantum anomalous Hall states in twisted MoTe₂, *Nature* **622**, 63 (2023).

[14] Y. Jia, J. Yu, J. Liu, J. Herzog-Arbeitman, Z. Qi, H. Pi, N. Regnault, H. Weng, B. A. Bernevig, and Q. Wu, Moir fractional Chern insulators. I. First-principles calculations and continuum models of twisted bilayer MoTe₂, *Physical Review B* **109**, 205121 (2024).

[15] C. Wang, X.-W. Zhang, X. Liu, Y. He, X. Xu, Y. Ran, T. Cao, and D. Xiao, Fractional Chern Insulator in Twisted Bilayer MoTe₂, *arXiv:2304.11864* [cond-mat].

[16] Y. Zeng, Z. Xia, K. Kang, J. Zhu, P. Knppel, C. Vaswani, K. Watanabe, T. Taniguchi, K. F. Mak, and J. Shan, Thermodynamic evidence of fractional Chern insulator in moir MoTe₂, *Nature* **622**, 69 (2023).

[17] T. Li, S. Jiang, B. Shen, Y. Zhang, L. Li, Z. Tao, T. Devakul, K. Watanabe, T. Taniguchi, L. Fu, J. Shan, and K. F. Mak, Quantum anomalous Hall effect from intertwined moir bands, *Nature* **600**, 641 (2021).

[18] L. Wang, E.-M. Shih, A. Ghiotto, L. Xian, D. A. Rhodes, C. Tan, M. Claassen, D. M. Kennes, Y. Bai, B. Kim, K. Watanabe, T. Taniguchi, X. Zhu, J. Hone, A. Rubio, A. N. Pasupathy, and C. R. Dean, Correlated electronic phases in twisted bilayer transition metal dichalcogenides, *Nature Materials* **19**, 861 (2020).

[19] T. Devakul, V. Crpel, Y. Zhang, and L. Fu, Magic in twisted transition metal dichalcogenide bilayers, *Nature Communications* **12**, 6730 (2021).

[20] N. Leconte, S. Javvaji, J. An, A. Samudrala, and J. Jung, Relaxation effects in twisted bilayer graphene: A multi-scale approach, *Physical Review B* **106**, 115410 (2022).

[21] S. Shabani, D. Halbertal, W. Wu, M. Chen, S. Liu, J. Hone, W. Yao, D. N. Basov, X. Zhu, and A. N. Pasupathy, Deep moir'e potentials in twisted transition metal dichalcogenide bilayers, *Nature Physics* **17**, 720 (2021), *arXiv:2008.07696* [cond-mat].

[22] N. Tilak, G. Li, T. Taniguchi, K. Watanabe, and E. Y. Andrei, Moir Potential, Lattice Relaxation, and Layer Polarization in Marginally Twisted MoS₂ Bilayers, *Nano Letters* **23**, 73 (2023).

[23] S. Carr, D. Massatt, S. B. Torrisi, P. Cazeaux, M. Luskin, and E. Kaxiras, Relaxation and domain formation in incommensurate two-dimensional heterostructures, *Physical Review B* **98**, 224102 (2018).

[24] N. Nakatsuji, T. Kawakami, and M. Koshino, Multi-scale Lattice Relaxation in General Twisted Trilayer Graphenes, *Physical Review X* **13**, 041007 (2023).

[25] J. Jung, A. M. DaSilva, A. H. MacDonald, and S. Adam, Origin of band gaps in graphene on hexagonal boron nitride, *Nature Communications* **6**, 6308 (2015).

[26] J. Jung, A. Raoux, Z. Qiao, and A. H. MacDonald, *Ab initio* theory of moir superlattice bands in layered two-dimensional materials, *Physical Review B* **89**, 205414 (2014).

[27] M. Koshino and N. N. T. Nam, Effective continuum model for relaxed twisted bilayer graphene and moir electron-phonon interaction, *Physical Review B* **101**, 195425 (2020).

[28] N. N. T. Nam and M. Koshino, Lattice relaxation and energy band modulation in twisted bilayer graphene, *Physical Review B* **96**, 075311 (2017).

[29] M. Koshino, N. F. Yuan, T. Koretsune, M. Ochi, K. Kuroki, and L. Fu, Maximally Localized Wannier Orbitals and the Extended Hubbard Model for Twisted Bilayer Graphene, *Physical Review X* **8**, 031087 (2018).

[30] W. Miao, C. Li, X. Han, D. Pan, and X. Dai, Truncated atomic plane wave method for subband structure calculations of moiré systems, *Physical Review B* **107**, 125112 (2023).

[31] S. J. Stuart, A. B. Tutein, and J. A. Harrison, A reactive potential for hydrocarbons with intermolecular interactions, *The Journal of Chemical Physics* **112**, 6472 (2000).

[32] W. Ouyang, D. Mandelli, M. Urbakh, and O. Hod, Nanoserpents: Graphene Nanoribbon Motion on Two-Dimensional Hexagonal Materials, *Nano Letters* **18**, 6009 (2018).

[33] A. N. Kolmogorov and V. H. Crespi, Registry-dependent interlayer potential for graphitic systems, *Physical Review B* **71**, 235415 (2005).

[34] M. H. Naik, I. Maity, P. K. Maiti, and M. Jain, KolmogorovCrespi Potential For Multilayer Transition-Metal Dichalcogenides: Capturing Structural Transformations in Moiré Superlattices, *The Journal of Physical Chemistry C* **123**, 9770 (2019).

[35] C. E. M. Nielsen, M. Da Cruz, A. Torche, and G. Bester, Accurate force-field methodology capturing atomic reconstructions in transition metal dichalcogenide moiré system, *Physical Review B* **108**, 045402 (2023).

[36] M. Long, P. A. Pantalen, Z. Zhan, F. Guinea, J. . Silva-Guilln, and S. Yuan, An atomistic approach for the structural and electronic properties of twisted bilayer graphene-boron nitride heterostructures, *npj Computational Materials* **8**, 73 (2022).

[37] J. Herzog-Arbeitman, Y. Wang, J. Liu, P. M. Tam, Z. Qi, Y. Jia, D. K. Efetov, O. Vafek, N. Regnault, H. Weng, Q. Wu, B. A. Bernevig, and J. Yu, Moiré fractional Chern insulators. II. First-principles calculations and continuum models of rhombohedral graphene superlattices, *Physical Review B* **109**, 205122 (2024).

[38] F. Haddadi, Q. Wu, A. J. Kruchkov, and O. V. Yazyev, Moiré Flat Bands in Twisted Double Bilayer Graphene, *Nano Letters* **20**, 2410 (2020).

[39] R. Jinnouchi, F. Karsai, and G. Kresse, On-the-fly machine learning force field generation: Application to melting points, *Physical Review B* **100**, 014105 (2019).

[40] A. Musaelian, S. Batzner, A. Johansson, L. Sun, C. J. Owen, M. Kornbluth, and B. Kozinsky, Learning Local Equivariant Representations for Large-Scale Atomistic Dynamics (2022), arXiv:2204.05249 [cond-mat, physics:physics].

[41] S. Batzner, A. Musaelian, L. Sun, M. Geiger, J. P. Maloa, M. Kornbluth, N. Molinari, T. E. Smidt, and B. Kozinsky, E(3)-equivariant graph neural networks for data-efficient and accurate interatomic potentials, *Nature Communications* **13**, 2453 (2022).

[42] H. Wang, L. Zhang, J. Han, and W. E, DeePMD-kit: A deep learning package for many-body potential energy representation and molecular dynamics, *Computer Physics Communications* **228**, 178 (2018).

[43] L. Zhang, J. Han, H. Wang, R. Car, and W. E, Deep Potential Molecular Dynamics: A Scalable Model with the Accuracy of Quantum Mechanics, *Physical Review Letters* **120**, 143001 (2018).

[44] J. Zeng, D. Zhang, D. Lu, P. Mo, Z. Li, Y. Chen, M. Rynik, L. Huang, Z. Li, S. Shi, Y. Wang, H. Ye, P. Tuo, J. Yang, Y. Ding, Y. Li, D. Tisi, Q. Zeng, H. Bao, Y. Xia, J. Huang, K. Muraoka, Y. Wang, J. Chang, F. Yuan, S. L. Bore, C. Cai, Y. Lin, B. Wang, J. Xu, J. Zhu, C. Luo, Y. Zhang, R. E. A. Goodall, W. Liang, A. K. Singh, S. Yao, J. Zhang, R. Wentzcovitch, J. Han, J. Liu, W. Jia, D. M. York, W. E, R. Car, L. Zhang, and H. Wang, DeePMD-kit v2: A software package for deep potential models, *The Journal of Chemical Physics* **159**, 054801 (2023).

[45] J. Behler and M. Parrinello, Generalized Neural-Network Representation of High-Dimensional Potential-Energy Surfaces, *Physical Review Letters* **98**, 146401 (2007).

[46] A. P. Bartk, M. C. Payne, R. Kondor, and G. Csnyi, Gaussian Approximation Potentials: The Accuracy of Quantum Mechanics, without the Electrons, *Physical Review Letters* **104**, 136403 (2010).

[47] K. T. Schtt, H. E. Sauceda, P.-J. Kindermans, A. Tkatchenko, and K.-R. Mller, SchNet A deep learning architecture for molecules and materials, *The Journal of Chemical Physics* **148**, 241722 (2018).

[48] R. Drautz, Atomic cluster expansion for accurate and transferable interatomic potentials, *Physical Review B* **99**, 014104 (2019).

[49] C. W. Park, M. Kornbluth, J. Vandermause, C. Wolverton, B. Kozinsky, and J. P. Mailoa, Accurate and scalable graph neural network force field and molecular dynamics with direct force architecture, *npj Computational Materials* **7**, 73 (2021).

[50] Y. Xie, J. Vandermause, L. Sun, A. Cepellotti, and B. Kozinsky, Bayesian force fields from active learning for simulation of inter-dimensional transformation of stanene, *npj Computational Materials* **7**, 40 (2021).

[51] C. Chen and S. P. Ong, A universal graph deep learning interatomic potential for the periodic table, *Nature Computational Science* **2**, 718 (2022).

[52] B. Deng, P. Zhong, K. Jun, J. Riebesell, K. Han, C. J. Bartel, and G. Ceder, Chgnet as a pretrained universal neural network potential for charge-informed atomistic modelling, *Nature Machine Intelligence* **5**, 1031 (2023).

[53] I. Batatia, P. Benner, Y. Chiang, A. M. Elena, D. P. Kovcs, J. Riebesell, X. R. Advincula, M. Asta, M. Avaylon, W. J. Baldwin, F. Berger, N. Bernstein, A. Bhowmik, S. M. Blau, V. Crare, J. P. Darby, S. De, F. D. Pia, V. L. Deringer, R. Eliojus, Z. El-Machachi, F. Falcioni, E. Fako, A. C. Ferrari, A. Genreith-Schriever, J. George, R. E. A. Goodall, C. P. Grey, P. Grigorev, S. Han, W. Handley, H. H. Heenen, K. Hermansson, C. Holm, J. Jaafar, S. Hofmann, K. S. Jakob, H. Jung, V. Kapil, A. D. Kaplan, N. Karimitari, J. R. Kermode, N. Kroupa, J. Kullgren, M. C. Kuner, D. Kuryla, G. Liepuoniute, J. T. Margraf, I.-B. Magdu, A. Michaelides, J. H. Moore, A. A. Naik, S. P. Niblett, S. W. Norwood, N. O'Neill, C. Ortner, K. A. Persson, K. Reuter, A. S. Rosen, L. L. Schaaf, C. Schran, B. X. Shi, E. Sivonxay, T. K. Stenczel, V. Svahn, C. Sutton, T. D. Swinburne, J. Tilly, C. v. d. Oord, E. Varga-Umbrich, T. Vegge, M. Vondrk, Y. Wang, W. C. Witt, F. Zills, and G. Csnyi, A foundation model for atomistic materials chemistry (2024), arXiv:2401.00096 [physics].

[54] K. Choudhary, B. DeCost, L. Major, K. Butler, J. Thiagaralingam, and F. Tavazza, Unified graph neural network force-field for the periodic table: solid state applications, *Digital Discovery* **2**, 346 (2023).

[55] C. Chen, W. Ye, Y. Zuo, C. Zheng, and S. P. Ong, Graph Networks as a Universal Machine Learning Framework for Molecules and Crystals, *Chemistry of Materials* **31**, 3564 (2019).

[56] F. Xie, T. Lu, S. Meng, and M. Liu, GPTFF: A high-accuracy out-of-the-box universal AI force field for arbitrary inorganic materials, *Science Bulletin* **69**, 3525 (2024).

[57] X. Liu, R. Peng, Z. Sun, and J. Liu, Moir Phonons in Magic-Angle Twisted Bilayer Graphene, *Nano Letters* **22**, 7791 (2022).

[58] X.-W. Zhang, C. Wang, X. Liu, Y. Fan, T. Cao, and D. Xiao, Polarization-driven band topology evolution in twisted MoTe₂ and WSe₂, *Nature Communications* **15**, 4223 (2024).

[59] Y. Zhang, H. Pi, J. Liu, W. Miao, Z. Qi, N. Regnault, H. Weng, X. Dai, B. A. Bernevig, Q. Wu, and J. Yu, Universal Moir-Model-Building Method without Fitting: Application to Twisted MoTe₂ and WSe₂ (2024), arXiv:2411.08108 [cond-mat].

[60] C. Xu, N. Mao, T. Zeng, and Y. Zhang, Multiple Chern bands in twisted MoTe₂ and possible non-Abelian states (2024), arXiv:2403.17003 [cond-mat].

[61] N. Mao, C. Xu, J. Li, T. Bao, P. Liu, Y. Xu, C. Felser, L. Fu, and Y. Zhang, Transfer learning relaxation, electronic structure and continuum model for twisted bilayer MoTe₂, *Communications Physics* **7**, 262 (2024).

[62] Y. Zhang, H. Wang, W. Chen, J. Zeng, L. Zhang, H. Wang, and W. E, DP-GEN: A concurrent learning platform for the generation of reliable deep learning based potential energy models, *Computer Physics Communications* **253**, 107206 (2020), arXiv:1910.12690 [physics].

[63] G. Kresse and J. Furthmiller, Efficient iterative schemes for *ab initio* total-energy calculations using a plane-wave basis set, *Physical Review B* **54**, 11169 (1996).

[64] A. P. Thompson, H. M. Aktulga, R. Berger, D. S. Bolintineanu, W. M. Brown, P. S. Crozier, P. J. in 't Veld, A. Kohlmeyer, S. G. Moore, T. D. Nguyen, R. Shan, M. J. Stevens, J. Tranchida, C. Trott, and S. J. Plimpton, LAMMPS - a flexible simulation tool for particle-based materials modeling at the atomic, meso, and continuum scales, *Comp. Phys. Comm.* **271**, 108171 (2022).

[65] A. H. Larsen, J. J. Mortensen, J. Blomqvist, I. E. Castelli, R. Christensen, M. Dulak, J. Friis, M. N. Groves, B. Hammer, C. Hargus, *et al.*, The atomic simulation environment a python library for working with atoms, *Journal of Physics: Condensed Matter* **29**, 273002 (2017).

[66] M. Dion, H. Rydberg, E. Schrder, D. C. Langreth, and B. I. Lundqvist, Van der Waals Density Functional for General Geometries, *Physical Review Letters* **92**, 246401 (2004).

[67] J. Klime, D. R. Bowler, and A. Michaelides, Van der Waals density functionals applied to solids, *Physical Review B* **83**, 195131 (2011).

[68] J. Klime, D. R. Bowler, and A. Michaelides, Chemical accuracy for the van der Waals density functional, *Journal of Physics: Condensed Matter* **22**, 022201 (2010).

[69] K. Berland and P. Hyldgaard, Exchange functional that tests the robustness of the plasmon description of the van der Waals density functional, *Physical Review B* **89**, 035412 (2014).

[70] R. Sabatini, T. Gorni, and S. De Gironcoli, Nonlocal van der Waals density functional made simple and efficient, *Physical Review B* **87**, 041108 (2013).

[71] H. Peng, Z.-H. Yang, J. P. Perdew, and J. Sun, Versatile van der Waals Density Functional Based on a Meta-Generalized Gradient Approximation, *Physical Review X* **6**, 041005 (2016).

[72] J. Ning, M. Kothakonda, J. W. Furness, A. D. Kaplan, S. Ehlert, J. G. Brandenburg, J. P. Perdew, and J. Sun, Workhorse minimally empirical dispersion-corrected density functional with tests for weakly bound systems: r 2 SCAN + rVV 10, *Physical Review B* **106**, 075422 (2022).

[73] I. Hamada, van der Waals density functional made accurate, *Physical Review B* **89**, 121103 (2014).

[74] K. Lee, . D. Murray, L. Kong, B. I. Lundqvist, and D. C. Langreth, Higher-accuracy van der Waals density functional, *Physical Review B* **82**, 081101 (2010).

[75] S. Grimme, Semiempirical GGAtype density functional constructed with a longrange dispersion correction, *Journal of Computational Chemistry* **27**, 1787 (2006).

[76] S. Grimme, J. Antony, S. Ehrlich, and H. Krieg, A consistent and accurate *ab initio* parametrization of density functional dispersion correction (DFT-D) for the 94 elements H-Pu, *The Journal of Chemical Physics* **132**, 154104 (2010).

[77] S. Grimme, S. Ehrlich, and L. Goerigk, Effect of the damping function in dispersion corrected density functional theory, *Journal of Computational Chemistry* **32**, 1456 (2011).

[78] A. Tkatchenko and M. Scheffler, Accurate Molecular Van Der Waals Interactions from Ground-State Electron Density and Free-Atom Reference Data, *Physical Review Letters* **102**, 073005 (2009).

[79] T. Gould, S. Lebgue, J. G. ngyn, and T. Boko, A Fractionally Ionic Approach to Polarizability and van der Waals Many-Body Dispersion Calculations, *Journal of Chemical Theory and Computation* **12**, 5920 (2016).

[80] T. Gould and T. Boko, C_6 Coefficients and Dipole Polarizabilities for All Atoms and Many Ions in Rows 16 of the Periodic Table, *Journal of Chemical Theory and Computation* **12**, 3603 (2016).

[81] H. Kim, J.-M. Choi, and W. A. Goddard, Universal Correction of Density Functional Theory to Include London Dispersion (up to Lr, Element 103), *The Journal of Physical Chemistry Letters* **3**, 360 (2012).

[82] S. N. Steinmann and C. Corminboeuf, Comprehensive Benchmarking of a Density-Dependent Dispersion Correction, *Journal of Chemical Theory and Computation* **7**, 3567 (2011).

[83] M. Hellenbrandt, The inorganic crystal structure database (icsd)present and future, *Crystallography Reviews* **10**, 17 (2004).